







Doppler coherence imaging of scrape-off-layer impurity flows in the HL-2A tokamak

Cite as: Rev. Sci. Instrum. **91**, 083504 (2020); <https://doi.org/10.1063/5.0005609>

Submitted: 22 February 2020 . Accepted: 24 July 2020 . Published Online: 06 August 2020

 T. Long, J. S. Allcock,  L. Nie,  R. M. Sharples, M. Xu,  R. Ke, S. Zhang, S. A. Silburn, J. Howard,  Y. Yu, B. Yuan,  Z. H. Wang, X. M. Song, L. Liu, and X. R. Duan



View Online



Export Citation



CrossMark

ARTICLES YOU MAY BE INTERESTED IN

[Preparation, analysis, and application of coated glass targets for the Wendelstein 7-X laser blow-off system](#)

Review of Scientific Instruments **91**, 083503 (2020); <https://doi.org/10.1063/1.5144943>

[Calibration of T-shaped atomic force microscope cantilevers using the thermal noise method](#)

Review of Scientific Instruments **91**, 083703 (2020); <https://doi.org/10.1063/5.0013091>

[Performance of the newly installed vertical neutron cameras for low neutron yield discharges in the Large Helical Device](#)

Review of Scientific Instruments **91**, 083505 (2020); <https://doi.org/10.1063/5.0010302>

Meet the Next Generation
of Quantum Analyzers

And Join the Launch
Event on November 17th



Register now



Zurich
Instruments



Doppler coherence imaging of scrape-off-layer impurity flows in the HL-2A tokamak

Cite as: Rev. Sci. Instrum. 91, 083504 (2020); doi: 10.1063/5.0005609

Submitted: 22 February 2020 • Accepted: 24 July 2020 •

Published Online: 6 August 2020



View Online



Export Citation



CrossMark

T. Long,¹  J. S. Allcock,^{2,3} L. Nie,^{1,a)}  R. M. Sharples,²  M. Xu,¹ R. Ke,¹  S. Zhang,^{1,4} S. A. Silburn,³ J. Howard,⁵ Y. Yu,⁴  B. Yuan,^{1,4} Z. H. Wang,¹  X. M. Song,¹ L. Liu,¹ and X. R. Duan¹

AFFILIATIONS

¹Southwestern Institute of Physics, Chengdu 610041, China

²Centre for Advanced Instrumentation, Department of Physics, Durham University, Durham DH1 3LE, United Kingdom

³Kingdom Atomic Energy Authority, Culham Centre for Fusion Energy, Culham Science Centre, Abingdon, Oxon OX14 3DB, United Kingdom

⁴University of Science and Technology of China, Hefei 230026, China

⁵Australian National University, Canberra, ACT 0200, Australia

^{a)} Author to whom correspondence should be addressed: nielin@swip.ac.cn

ABSTRACT

A new Doppler coherence imaging spectroscopy interferometer has been developed on the HL-2A tokamak for the scrape-off-layer impurity flow measurement. Its spatial resolution is estimated to be up to ~ 0.8 mm in the horizontal direction and ~ 9 mm in the vertical direction, with a field of view of $\sim 34^\circ$. Its typical temporal resolution is about 1 ms. This salient feature allows for time-resolved 2D measurements in short-time phenomena on HL-2A, such as edge localized modes. Group delay and interference fringe pattern were calibrated with a dedicated calibration system. The robustness of group delay calibration and the feasibility of the extrapolation model for fringe pattern calibration are demonstrated. In this paper, we report the details of the optical instruments, calibration, and the initial experimental results of this Doppler coherence imaging spectroscopy interferometer.

Published under license by AIP Publishing. <https://doi.org/10.1063/5.0005609>

I. INTRODUCTION

Impurity issue is a significant concern for burning-plasma devices, particularly because excessive impurity will limit the fusion reaction rate via dilution. The resulting radiative cooling can cause plasma disruption,¹ which is also one of the top risks for fusion reactors, such as International Thermonuclear Experimental Reactor (ITER). Impurity content in the plasma scrape-off layer (SOL) has serious effects on the erosion and deposition of plasma-facing materials.² The radial profile of impurity flows in the SOL changes with poloidal location due to the mechanism of classical drifts and asymmetry in radial diffusion.³ These flows in the SOL play important roles in the asymmetric distribution of power on the inner and outer divertors.⁴⁻⁶ Besides, SOL flows impose the boundary conditions on the confined plasma and are closely related to pedestal instabilities and the resulting edge turbulence transport. Thus, a two-dimensional measurement of impurity flows is important to

study impurity transport behaviors⁷ and the related physical problems. For example, what is the role of these flows in the sensitivity of L-H power threshold to X-point location?^{2,8} How does the flow pattern change during the edge localized mode (ELM) crash events?⁹ What is their relation to the ELM mitigation by resonant magnetic perturbation (RMP) fields?^{10,11} Doppler Coherence Imaging Spectroscopy (CIS)^{12,13} provides a useful diagnostic technique to measure the time-resolved impurity flows in the plasma boundary.

Static modulated polarization interferometer for coherence imaging of plasma parameters was firstly developed as a fusion diagnostic by Howard.^{14,15} The spectral information is encoded on the spatial heterodyne carriers of the interference image. The physical parameters of emitting species can be obtained from the relationship between fringe visibility and velocity distribution function of emission. The major advantages of this interferometer (spectrometer) over the conventional grating-based spectrometer are

the high throughput and the ability of 2D measurements. The applications of the coherence imaging technique in the magnetic confinement plasmas include (a) Doppler CIS (Doppler shift and broadening) for intensity, flow velocity, and temperature measurements; (b) polarization CIS (Zeeman and motional Stark effects) for magnetic field pitch angle and current density measurements;¹⁶ (c) Stark CIS (Stark broadening) for density measurements;¹⁷ and (d) relative line intensity for isotope abundance measurements.¹²

CIS techniques have been applied on various magnetic confinement devices, including linear device,¹⁸ dipole device,¹⁹ stellarators,^{20–22} and tokamaks.^{23–29} Doppler CIS measurements on the MAST tokamak show that counter-streaming flows of impurities²⁸ due to gas puffing increase the pressure on field lines. These results are reproduced by EMC3-EIRENE simulations.³⁰ The CIS diagnostic on the RT-1 device visualized the effect of the ion cyclotron resonance frequency heating on dipole plasma.¹⁹ The ion temperature and flow were enhanced globally, particularly along the magnetic field lines near the levitation magnet.¹⁹ Stokes–Doppler coherence imaging has been designed as a routine diagnostic for ITER boundary tomography.³¹ Doppler coherence imaging technique may be able to be applied to other radiating inhomogeneous media, such as flames, auroras, and plasma thruster.

The measurement principles of Doppler CIS^{12,26} are based on the Fourier transform spectroscopy and the Doppler shifts of visible ion emission spectral lines. Considering that the monochromatic light passes through a two-beam interferometer with a time delay τ between these two beams, an interferogram with the sinusoidal fringe can be observed,

$$S(\tau) = \frac{I_0}{2} \{1 + \xi_D \cos(\phi_0 + \phi_D)\}. \quad (1)$$

Here, I_0 is the intensity of the light source. ξ_D denotes the contrast envelope of fringe. $\phi_0 = 2\pi\nu_0\tau_0$ represents the phase introduced from un-shifted time delay τ_0 . ν_0 is the optical frequency of the light in the plasma rest frame,

$$\phi_D = \kappa(\tau_0)\phi_0 \left(-\vec{v}_D \cdot \frac{\hat{l}}{c} \right). \quad (2)$$

ϕ_D represents the phase caused by the Doppler frequency shift due to line-of-sight plasma flow, where $\kappa(\tau_0)$ represents the delay dispersion of the birefringent crystal of the interferometer.¹² The orientation of a positive ν_D is directed from the plasma to detector. \hat{l} is a unit vector in the direction from the detector to plasma. Thus, the plasma flow velocity can be obtained via the Doppler phase of the fringe,

$$\vec{v}_D \cdot \hat{l} = -\frac{c\phi_D}{\kappa(\tau_0)\phi_0}. \quad (3)$$

The remainder of this paper is organized as follows. We introduce the Doppler CIS diagnostic system on the HL-2A tokamak, including the optical system in Sec. II and the calibration system in Sec. III. In Sec. II, the details of optical path and optical instruments are presented. In Sec. III, the calibration instruments and calibration results are displayed. Section IV reports the Doppler CIS experimental measurements in an ELMy H-mode discharge. Section V gives the summary and discussion.

II. THE OPTICAL SYSTEM OF DOPPLER CIS FOR HL-2A

HL-2A tokamak is a medium-size magnetic confinement device, with a major radius of 1.65 m and a minor radius of 0.4 m.³² It operates with $B_t < 2.7$ T. The viewing window of Doppler CIS on HL-2A is made of quartz, and its diameter is ~ 105 mm. The center of the port is located at ~ 200 mm above the midplane of the low field side. A stainless-steel shutter is installed in front of the window. This is to prevent the window from coating during glow discharge cleaning and silicization of the vacuum vessel. The detector is a high-speed camera, which must be at least 3 m away from the magnetic field coils to be free from the electromagnetic interference. Thus, an optical system was designed for Doppler CIS diagnostic on the HL-2A tokamak, as shown in Fig. 1. The simulated light path is represented by the colored line beams.

A mirror (120×100 mm², reflectivity $> 95\%$) near the viewing port is used to reflect the light emitted from plasma. All the lenses in the optical system are the standard commercial lenses.³³ Lens 1 is Sigma 70 mm–200 mm F2.8 DG OS HSM F-Mount zoom lens. Its focal length is 70 mm–200 mm. Its F number is 2.8. Lens 2 and Lens 3 are two Sigma 500 mm F4 DG OS HSM F-Mount prime lenses. The focal length is 500 mm. The F number is 4. Lens 4 and Lens 5 are two Sigma 150 mm F2.8 EX DG OS HSM F-Mount prime lenses. The focal length is 150 mm. The F number is 2.8. Lens 1 views the

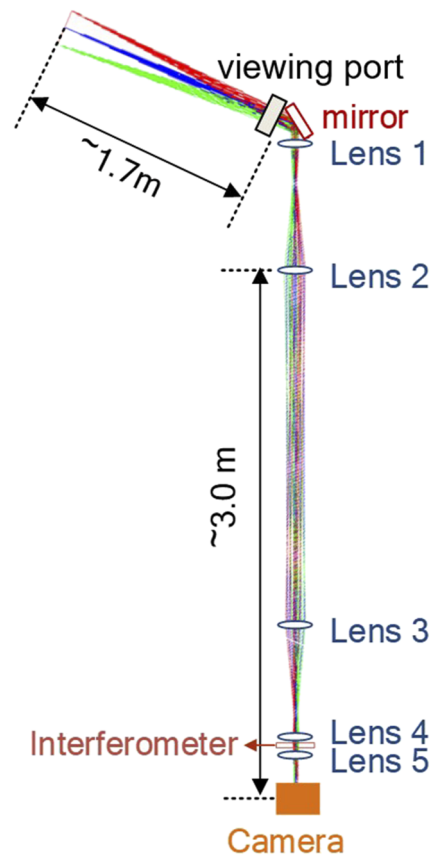


FIG. 1. A schematic of the Doppler CIS optical system on the HL-2A tokamak.

plasma through the mirror and forms a demagnified plasma image. The light is then collimated by placing this image at the detector plane of Lens 2 with its focus set to infinity. Lens 3 views the collimated light and forms the image again. Lens 2 and Lens 3 are used to relay the optical path. The light is again collimated by placing the image at the detector plane of Lens 4 with its focus set to infinity. The CIS interferometer lies in the collimated light region between Lens 4 and Lens 5. Lens 5 views the light passing through the interferometer and forms an interferogram image on the sensor of the camera.

This static polarization interferometer is the key part of CIS diagnostic. Compared with the traditional Michelson interferometer, it is more stable and has a higher time resolution. The traditional Michelson interferometer is based on temporal multiplexing techniques. It generally scans the phase delay by installing a movable mirror on one arm of the interferometer to change the path length of the arm.³⁴ These systems are highly sensitive to mirror vibrations. They have been widely applied in space-based astronomical and remote sensing applications, where variations of the source spectrum are slow, and long scanning times (1 s–10 s) are, therefore, acceptable. The static polarization interferometer is based on spatial multiplexing techniques. The phase delay is varied in space (along one detector dimension). This allows the entire interferogram to be recorded simultaneously with high time resolution (~ms).

A schematic of the CIS interferometer is shown in Fig. 2(a). It is composed of four plates with a diameter of ~2 in. They are a polarizer, a wave plate (delay plate), a Savart plate, and an analyzer, respectively. The polarizer and analyzer are Newport 20LP-VIS polarizers. The extinction ratio is 25 000:1. The delay plate and Savart plate are manufactured by CLaser Photonics. They are made from the alpha barium borate (BaB_2O_4 , α -BBO) birefringent crystal with anti-reflection coating. The Savart plate is composed of two equal-thickness (“ t ”) plates cemented together, each with their optic axes at 45° to the surface normal and rotated through 90° with respect to each other, as shown in Fig. 2(b). The designed manufacturing thickness of the delay plate is 4.6 mm and 4.0 mm for the Savart plate, with the tolerance of ± 0.3 mm.

The collimated light beam becomes polarized after passing through the polarizer. Then, it is resolved into two components in the wave plate. They are an ordinary (O) component polarized parallelly to the wave plate’s optic axis and an extraordinary (E) component polarized perpendicularly. A fixed phase delay ϕ_d is introduced by the wave plate due to the different refractive indexes between the O and E components. Then, the Savart plate is used to split the O and E components spatially.³⁵ The vertical spatial distance of the O and E components is “ d ,” as shown in Fig. 2(b). The Savart plate imposes an additional phase delay ϕ_s , which depends on the incident angle of light. The light beams are converged by Lens 5. They eventually interfere at the image plane. The angle-dependent delay sweeping leads to the interferogram.

The light intensity can be extracted from the interferogram by filtering out the carrier fringe frequency in the Fourier domain. The instantaneous phase can, then, be extracted from the fringe pattern by a demodulation technique based on the discrete Fourier transform.³⁶ The fringe pattern is sensitive to ambient temperature due to the thermal expansion effect. It is also sensitive to the alignment of birefringent plates. Therefore, all plates are fastened tightly and enclosed in an Andover 101FRDC00-CTRL temperature controller.

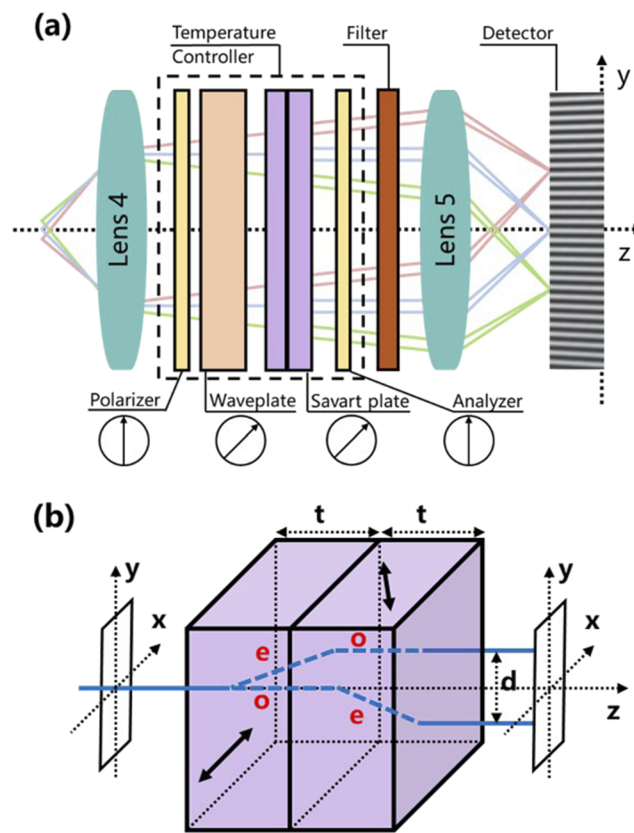


FIG. 2. (a) A schematic of the CIS polarization interferometer and (b) the construction and operation of the Savart plate.

The regulation range is 30°C – 60°C , and the regulation accuracy is $\pm 0.2^\circ\text{C}$. Besides, Lens 4, Lens 5, the interferometer, and camera are all installed on a long straight rail. The custom optical tables have been firmly fixed on the concrete floors in the lab or next to tokamak. Hence, this rail can be fixed on these tables to shield low-frequency mechanical vibrations.

A custom bandpass filter in front of Lens 5 is used to isolate the target spectral line. Since the divertor of the HL-2A tokamak is covered with a carbon fiber composite material, CIII triplet lines emitted from impurity ions C^{2+} are very strong. There are no conspicuous contaminations from other spectral lines in the neighborhood. These are beneficial for the Doppler CIS measurement. Therefore, the CIII triplet is used as the target line. The wavelengths of CIII triplet lines are 464.742 nm, 465.025 nm, and 465.147 nm, respectively. The normalized relative intensity $I_n / \sum_n I_n$ of each line is 0.556, 0.333, and 0.111, according to the calculations based on the NIST atomic spectra database.³⁷ Thus, the calculated intensity weighted average wavelength $\sum_n I_n \lambda_n / \sum_n I_n$ of the CIII triplet is 464.88 nm. To verify the result, a visible spectrometer on the HL-2A tokamak³⁸ was used to measure the CIII triplet spectrum. This spectrometer viewed the plasma radially with its sight lines straight toward the center solenoid on the midplane. Multiple measurements were made under different discharge conditions. Variations between

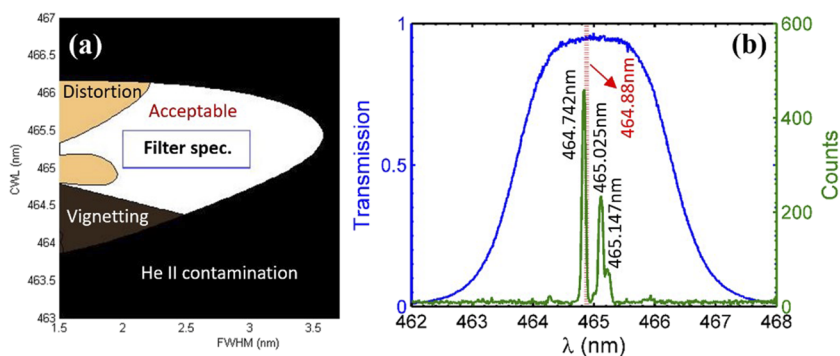


FIG. 3. (a) Bandpass filter specification for CIII lines in the parameter space: CWL vs FWHM; (b) the transmission profile of the custom filter and the measured spectra on the HL-2A tokamak.

the measurements are small. One measurement of the CIII triplet spectrum is shown by the green line in Fig. 3(b). The measured intensity weighted average wavelength is about 464.88 nm. The measured and the calculated average wavelengths are found to be in good agreement, which indicates that the multiple structure of CIII lines can be considered constant.

Figure 3(a) shows the filter performance over two parameters. They are center wavelength (CWL) and full width at half maximum (FWHM) of the filter's transmission profile. The performance in the white region is acceptable for CIS measurements. It shows a

high transmission, slight phase distortions between the image core and the edge, weak neighboring lines' contamination, and negligible vignetting. This calculation is based on Ref. 36 where more details can be found. In Fig. 3(b), the green line shows the measured CIII triplet spectra on the HL-2A tokamak. The red dotted line indicates the CIII average wavelength. The blue line shows the transmission profile of the filter.

A Phantom v2012 high-speed camera is used to image the interferogram. The camera sensor is a CMOS (Complementary Metal-Oxide-Semiconductor) sensor. The quantum efficiency in

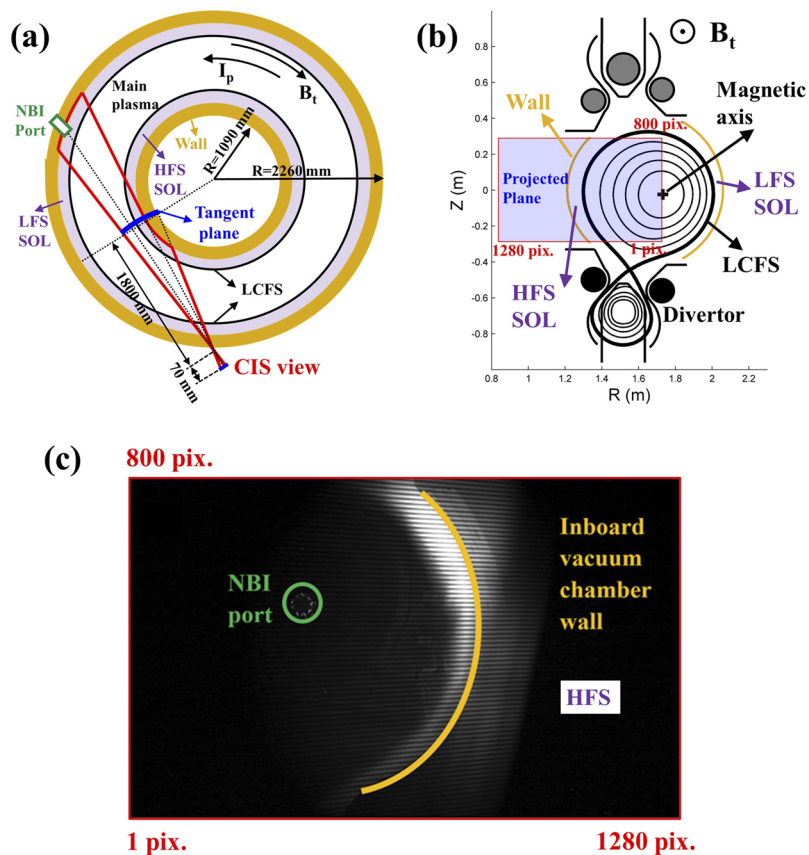


FIG. 4. (a) The top view for the CIS field of view on the HL-2A tokamak, (b) the focused tangent plane's projection on the poloidal cross section, and (c) a CIS raw image in an H-mode discharge.

the 450 nm–500 nm range is about 45%. The bit depth is 12 to allow a high dynamic range. The sensor size is $35.8 \times 22.4 \text{ mm}^2$. The sensor pixel size is big ($28 \times 28 \mu\text{m}^2$), so it has high light sensitivity. The frame rate capability ranges from 100 Hz–22 500 Hz with the full resolution of $1280 \times 800 \text{ pixel}^2$. The temporal resolution can, therefore, range from 0.05 ms to 10 ms.

The typical temporal resolution achieved with the optical system above is about 1 ms with the full pixel resolution. This is much higher than the time resolution of Doppler CIS systems viewing SOL on other conventional tokamaks.^{24,29,39} This feature allows for time-resolved 2D measurements in short-time phenomena on the HL-2A tokamak, such as ELMs.

Figure 4(a) shows the top view of the field of view of Doppler CIS on the HL-2A tokamak. LFS denotes the low magnetic field side, and HFS denotes the high magnetic field side. SOL denotes the plasma scrape-off layer region outside the last closed flux surface (LCFS). The viewing angle is around 34° . The CIS focusing distance is $\sim 1800 \text{ mm}$. The focused tangent plane is marked with the blue curve in Fig. 4(a). This tangent plane is a curved surface normal to the lines of sight. Although the CIS system collects the light along the sight lines, the obtained images are dominated by light emitted close to this surface. According to the setup of the CIS optical path, we calculate that the field depth of the CIS system is $\sim 100 \text{ mm}$. The object within the field depth will all have a sharp image in the image plane.

Figure 4(b) shows the projection of the tangent plane on the poloidal cross section obtained by the equilibrium configuration reconstruction from EFIT code.⁴⁰ The size of the projection area is about $927 \times 580 \text{ mm}^2$. The inboard vacuum chamber wall on the HFS is inside this area. The field depth of $\sim 100 \text{ mm}$ corresponds to a sharply imaged object plane of $\sim 902 \times 564 \text{ mm}^2$ in front of this focused plane and a sharply imaged object plane of $\sim 954 \times 597 \text{ mm}^2$ behind this focused plane. As the image plane is $1280 \times 800 \text{ pixel}^2$, the dimension of the object corresponding to one pixel of the image is $\sim 0.8 \text{ mm}$. The spatial resolution in the horizontal direction is, then, estimated to be up to $\sim 0.8 \text{ mm}$. The spatial resolution in the vertical direction is determined by the scale of fringes, which is $\sim 11 \text{ pixels/fringe}$. Hence, the spatial resolution in the vertical direction is estimated to be up to $\sim 9 \text{ mm}$. Figure 4(c) shows a CIS raw image in an H-mode discharge. Note that the left and right sides of this image are opposite to Fig. 4(b). The inboard vacuum chamber wall and neutral beam injection (NBI) port can be seen in the image.

III. THE CALIBRATION SYSTEM OF DOPPLER CIS FOR HL-2A

As shown in Eq. (3), the flow velocity can be obtained from the phase shift of the interference fringe pattern relative to the fringe pattern produced by stationary emission. Equation (3) can be written as Eq. (4). $\phi(\lambda_0)$ is the phase of the fringe pattern without the Doppler shift. ϕ_m is the phase of the fringe pattern with the Doppler shift in the measurements. $\hat{N}(\lambda_0) = \kappa(\tau_0)v_0\tau_0$ is the group delay of the birefringent crystal in the interferometer at target line λ_0 . Group delay is often used in interferometry as a first-order approximation for instrument dispersion.³⁴ Calibration of the un-shifted fringe pattern, i.e., fringes generated from a motionless light source, and calibration of the group delay at λ_0 are both vital to obtain the flow velocity. With linear approximation,^{39,41} the normalized phase

shift is proportional to the normalized wavelength shift. Equation (5) follows directly from the definition of the group delay. $\hat{N}(\lambda_0)$ can be calibrated by fitting the $\Delta\phi/2\pi$ vs $(\lambda_0 - \lambda)/\lambda_{\text{line}}$,

$$\phi_D = \phi_m - \phi(\lambda_0) = 2\pi\hat{N}(\lambda_0)\frac{v_D}{c}, \quad (4)$$

$$\frac{\Delta\phi}{2\pi} = \frac{\phi(\lambda) - \phi(\lambda_0)}{2\pi} = \hat{N}(\lambda_0)\frac{\lambda_0 - \lambda}{\lambda}. \quad (5)$$

A dedicated calibration system has been designed and applied in the laboratory, as shown in Fig. 5. The light source is a New Focus Vantage tunable diode laser. The product number is TLB-7102. The output power is greater than 5 mW. It features mode-hop free wavelength tuning around CIII triplet lines. The accuracy of wavelength adjustment is around 1 pm. It is feasible to use it to simulate the CIII spectral line with or without the Doppler shift. A Newport 10FC16PB.3 polarizing cube beam splitter is used to split the laser beam into two beams. Their intensity ratio can be adjusted by rotating the Newport 10RP02-10 quartz half-wave plate. One beam is coupled to a high precision wavelength meter (HighFinesse WS6-200) via a built-in fiber of the wavelength meter. The wavelength measurement range of this wavelength meter is 330 nm–1180 nm. The accuracy of this wavelength meter is $\sim 0.1 \text{ pm}$. Another beam illuminates a Newport 819D-SF-6 modular integrating sphere and outputs a uniform circular light source. It generates a calibration interferogram at a certain wavelength via the CIS interferometer.

Figure 6(a) shows the wrapped phase demodulated from the interference fringe pattern at 464.88 nm, i.e., $\phi(\lambda_0)$. Figure 6(b) shows the calibration result for group delay $\hat{N}(\lambda_0)$. The range of wavelengths used here is [461.6, 466.1] nm. The demodulated phase shift $\Delta\phi$ for each wavelength shift is the average of phase shifts over the central image of $50 \times 50 \text{ pixel}^2$. It is marked with the blue rectangular point in Fig. 6(b). $\hat{N}(\lambda_0) = 1394.5$ is obtained via a polynomial fit (green dashed line) of these points. The red rhombic points show the theoretical results based on the Sellmeier equations.⁴² The theoretical group delay for an α -BBO wave plate with the thickness of 4.6 mm is 1439.4. The fitting result from the actual measurements is different from the theoretical result. This demonstrates that the actual thickness of the wave plate is not 4.6 mm due to the manufacturing tolerance. The thickness tolerance of $\pm 0.3 \text{ mm}$ corresponds to a group delay uncertainty of about ± 100 , which will increase the velocity measurement error. Since the demodulated phase is wrapped into $(-\pi, \pi]$, thus, $|\phi_D|$ should be smaller than π to get rid of phase jump. Substituting this into Eq. (4), the largest line-averaged flow velocity that can be measured is $|v_{\text{max}}| \approx 108 \text{ km/s}$. This is much larger than the flow velocity in the SOL region measured by probes. Therefore, there will not be a phase jump problem for this system.

The fringe pattern is sensitive to the change in the ambient temperature of birefringent crystals.^{36,41} Figure 7(a) shows the estimation of the phase drift due to the ambient temperature drift. After preheating the light source for 30 min, multiple measurements were made. The temperature of the interferometer temperature controller was set to be stable at 35.0°C during the whole measurements. The phase drift caused by the subtle temperature drift, which the temperature controller cannot notify, was converted to the velocity drift via

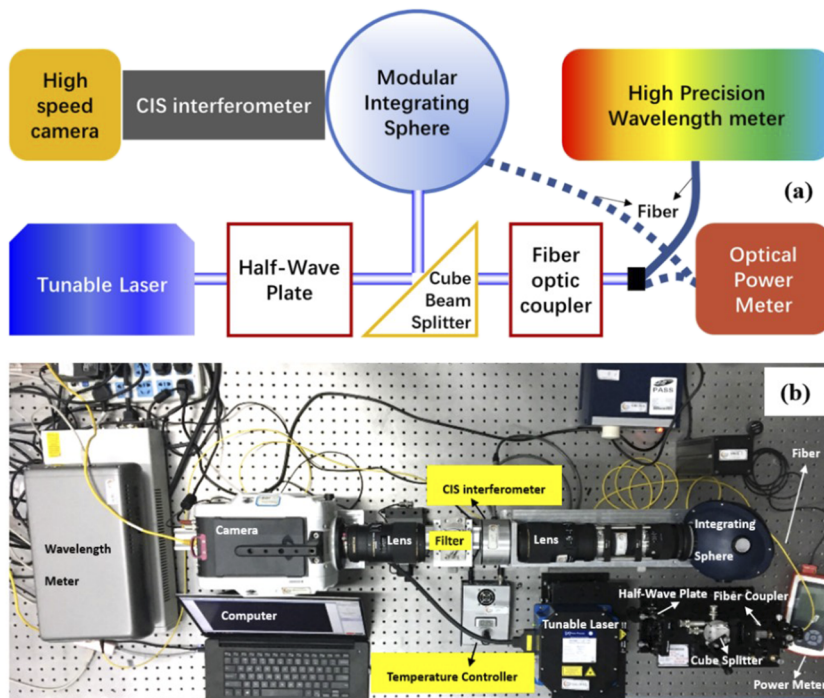


FIG. 5. (a) A schematic and (b) a photo of the CIS calibration system in the lab.

Eq. (4), by taking the first measurement as a reference. Figure 7(a) shows that this velocity drift is within 0.2 km/s.

To avoid the systematic error in the inferred flow, the instrument temperature must be stabilized, and the phase must be calibrated regularly. Unfortunately, it is not available to install the above laser calibration system in the HL-2A hall for the moment. An alternative calibration procedure for the fringe pattern is necessary. Here, the calibration technique we rely on is similar to the previous work.^{36,41} Group delay is still calibrated in the lab, while the fringe pattern is calibrated on the tokamak. Fringe pattern calibration is obtained via an extrapolation model of the fringe pattern measured at a nearby spectral line to the target line for a given interferometer, camera, and lens focal length, as shown in Eq. (6).³⁶ Besides, as CIII triplet lines are not monochromatic, a fixed phase offset (2.8086 rad)

due to the triplet lines has been considered,³⁶

$$\phi_{extrap}(x, y, \lambda_0) \approx \left[\frac{\lambda_1}{\lambda_0} \frac{n_0^2 + n_e^2}{n_0^2 - n_e^2} \bigg|_{\lambda_1} \frac{n_0^2 - n_e^2}{n_0^2 + n_e^2} \bigg|_{\lambda_0} \right] \phi(x, y, \lambda_1). \quad (6)$$

The group delay calibration in the lab remains valid for the measurements on HL-2A. Figure 7(b) shows the calibration results for the group delay after three different installations. The time between the first calibration and the third calibration is 7 days. $\hat{N}(\lambda_0) = 1394.9 \pm 0.6$ was obtained in the lab for the first calibration. Here, 0.6 is given by the polynomial fitting error. $\hat{N}(\lambda_0) = 1394.2 \pm 0.6$ was obtained after the interferometer was removed from the rail and installed on the rail again. $\hat{N}(\lambda_0) = 1394.5 \pm 0.4$ was obtained after the interferometer along with the rail was moved to the tokamak for the optical test and installed in the lab again. These results suggest that the group delay is not sensitive to the installation error. The relative error of the group delay is about 0.1%, which is very small. Therefore, calibration for the group delay is robust for the CIS measurement on HL-2A.

For the fringe pattern calibration, the phase error due to extrapolation of the fringe pattern is given by the phase difference $\phi_{extrap}(x, y, \lambda_0) - \phi(x, y, \lambda_0)$. Here, $\phi_{extrap}(x, y, \lambda_0)$ was calculated by extrapolating the fringe pattern at a nearby line λ_1 to the target line λ_0 , via Eq. (6). The fringe pattern at the nearby line $\phi(x, y, \lambda_1)$ was measured by using the tunable laser at $\lambda_1 = 461.91$ nm. The fringe pattern at the target line $\phi(x, y, \lambda_0)$ was measured by using the tunable laser at $\lambda_0 = 464.88$ nm. The phase error due to extrapolation of the fringe pattern is shown in Fig. 7(c). The phase error of extrapolation over 2.97 nm wavelength is within

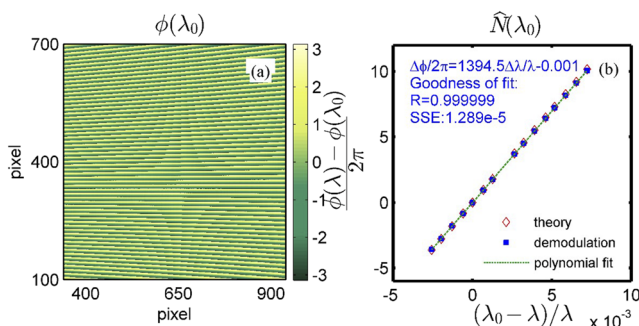


FIG. 6. (a) The fringe pattern of the CIII line at 464.88 nm, i.e., $\phi(\lambda_0)$ and (b) calibration for $\hat{N}(\lambda_0)$: the group delay of the birefringent crystal for the CIII line.

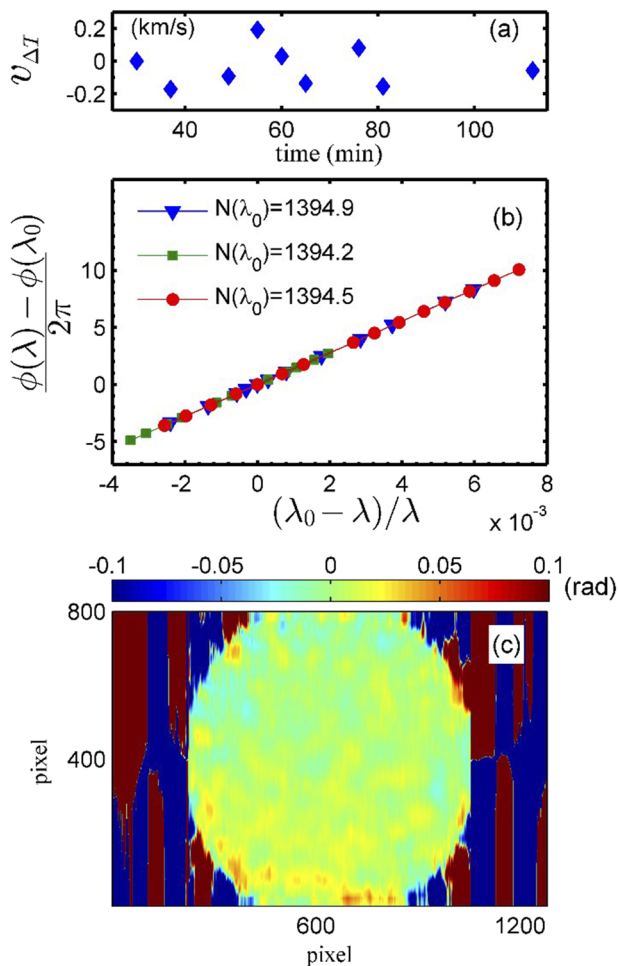


FIG. 7. (a) Phase drift due to the ambient temperature drift, (b) calibration results for the group delay after three different installations, (c) phase error due to extrapolation of the fringe pattern at a nearby line $\lambda_1 = 461.91$ nm to $\lambda_0 = 464.88$ nm.

~ 0.03 rad, which is corresponding to ~ 1.0 km/s. This result demonstrates the feasibility of the extrapolation model within the velocity error of ~ 1.0 km/s. Instead, a cadmium spectral lamp (at 467.81 nm) on the HL-2A tokamak was used for the fringe pattern calibration via extrapolation over 2.93 nm.

IV. DOPPLER CIS MEASUREMENTS IN AN ELMY H-MODE DISCHARGE

The Doppler CIS diagnostic was put into operation in the latest campaign (2018–2019) of the HL-2A tokamak. This system took raw images of the interferogram of CIII lines emitted from the plasma scrape-off layer of the high field side. Two-dimensional brightness images and phase images were extracted from the raw images. Combined with the calibration for the group delay and the fringe pattern without the Doppler shift, images of the C^{2+} sight-line-averaged flow velocity can be calculated by using Eq. (4). The typical frame rate is 1 kHz, which is limited by the light intensity.

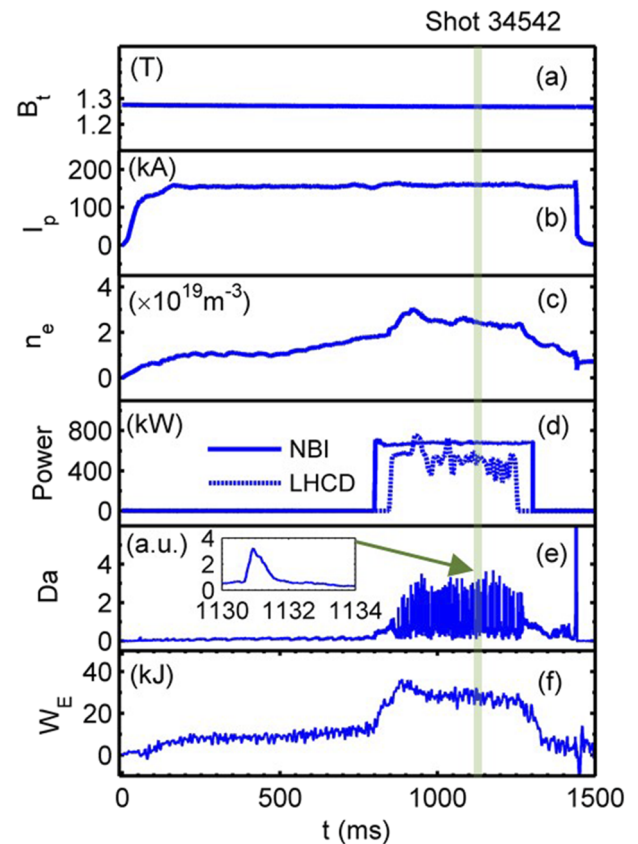


FIG. 8. An ELMy H-mode discharge on the HL-2A tokamak: (a) toroidal magnetic field, (b) plasma current, (c) central chord-averaged electron density, (d) auxiliary heating, (e) D_α signal in the divertor, and (f) stored energy.

Figure 8 shows an ELMy H-mode discharge with a lower single-null divertor configuration on the HL-2A tokamak. The discharge parameters are $B_t \sim 1.27$ T, $I_p \sim 160$ kA, and $\bar{n}_e \sim 2.0$ – $2.6 \times 10^{19} m^{-3}$. The lower hybrid current drive (LHCD) power is ~ 500 kW, and the NBI heating power is ~ 700 kW in the co-Ip direction. The plasma stored energy is 25 kJ–35 kJ.

Figure 9 shows 2D measurements by Doppler CIS during the time 1130 ms–1134 ms. This is corresponding to an ELM stage, as marked by the green rectangle in Fig. 8 or Fig. 10. The frame rate is 1 kHz, corresponding to the time resolution of 1 ms. Figures 9(a1)–9(a5) show the 2D images of line-integrated emissivity, $I_0 = \int e(r) dl$, where $e(r)$ is the local emissivity. Figures 9(b1)–9(b5) show the evolution of 2D images of the line-averaged flow velocity, $v_D = \int e(r) \bar{v}(r) \cdot d\hat{l} / I_0$, where $\bar{v}(r)$ is the local flow. $v_D > 0$ is corresponding to the co-Ip direction. $v_D < 0$ is corresponding to the counter-Ip direction. These show that the carbon flow velocity is $[-15, 15]$ km/s. The ELM crash started at a moment between 1130 ms and 1131 ms. From $t = 1130$ ms to $t = 1131$ ms, the CIII light intensity increases sharply and the carbon ion flow velocity increases in the co-Ip direction obviously, especially in the region above the midplane. A complicated flow pattern is found when looking at the whole cross section.

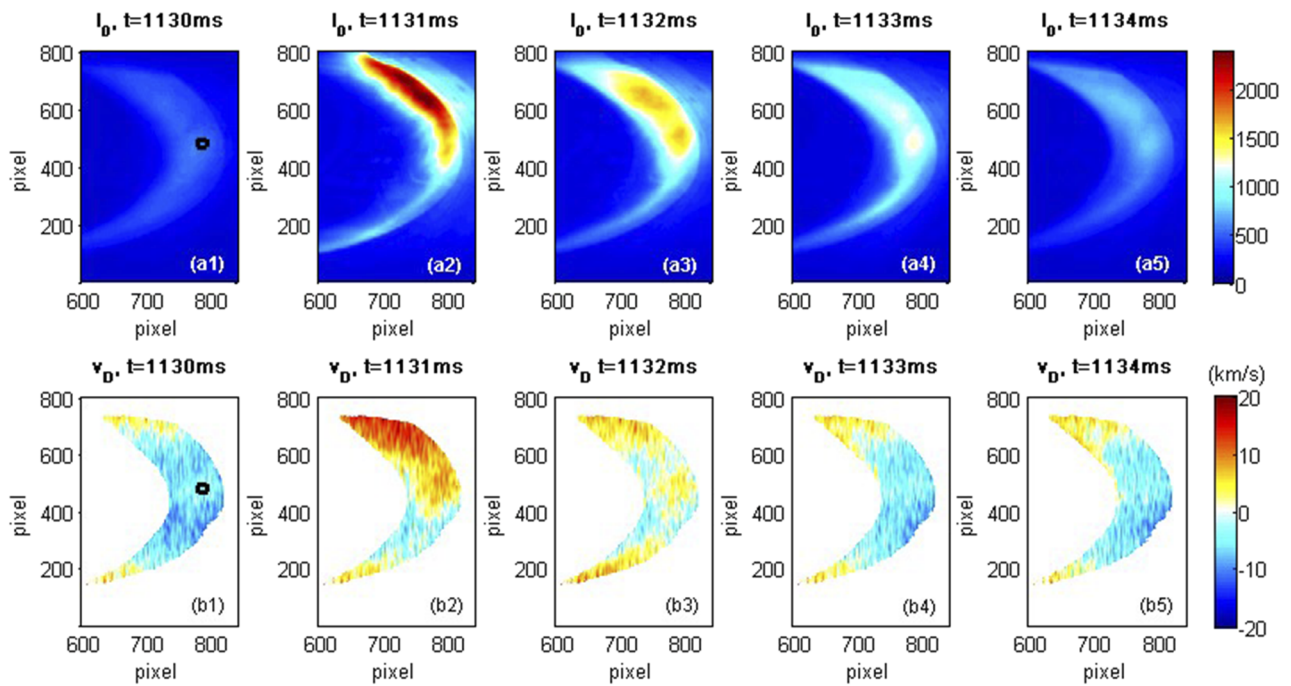


FIG. 9. Results for CIII emission and flow velocity measurements by Doppler CIS in an H-mode discharge on the HL-2A tokamak: (a1)–(a5) are the line-integrated emission images and (b1)–(b5) are the line-averaged flow velocity images, at an ELM stage.

At the time after the ELM crash ($t = 1134$ ms), the C^{2+} flow velocities in most areas above/below the midplane is negative. This is consistent with the projection of ion ∇B drift velocities on the CIS line of sight. Regarding the driving mechanism of ion flows in the SOL, the flow velocities are also affected by the ∇p drift, $E \times B$

drift, and the momentum transport.^{3,6} We cannot draw clear conclusions without measurements of plasma pressure, electric field, and momentum flux in the SOL. Besides, the asymmetry of the intensity and flow on the upper side and the lower side during an ELM crash may have some underlying correlations with the magnetic separatrix topology for the lower single-null divertor configuration. However, this needs further exploration, which is beyond the main scope of this article.

Figure 10(a) shows the time trace of the CIII light intensity in the area marked by the black rectangle in Fig. 9(a1), over a series of ELMs. It exhibits a similar trend with the D_α signal in the divertor. Figure 10(b) shows the time trace of the C^{2+} flow velocity in the same area. The rapid velocity variation of ~ 10 km/s in the co- I_p direction coincides with ELM crashes. The error bar (1 km/s–2 km/s), here, is estimated from the error introduced by phase calculation and group delay calibration. From Eq. (4), $v_D = c\phi_D/2\pi\dot{N}$, where $\phi_D = \phi_m - \phi(\lambda_0)$. Thus, the standard deviation of Doppler velocity $S_{v_D} = |v_D| \sqrt{(S_{\phi_m}^2 + S_{\phi(\lambda_0)}^2)/\phi_D^2 + S_{\dot{N}}^2/\dot{N}^2}$. $S_{\phi_m} \sim [0.002, 0.02]$ is the error introduced by image noise of the measured interferogram. $S_{\phi(\lambda_0)} \sim 0.03$ is the error introduced by the phase calibration of the fringe pattern. $S_{\dot{N}} \sim 1.0$ is the error introduced by the group delay calibration.

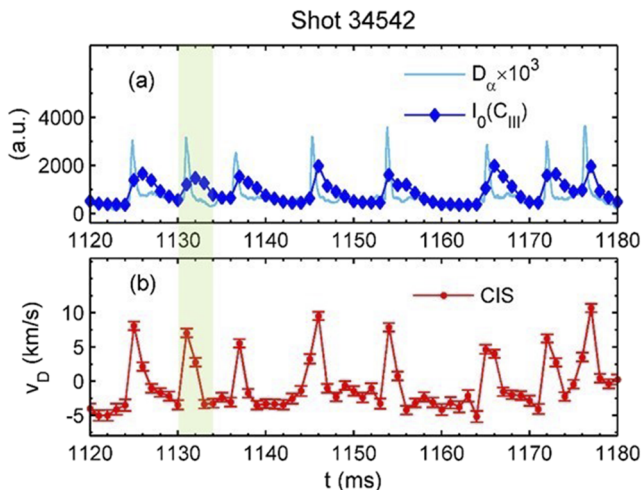


FIG. 10. (a) The time trace of the D_α signal in the divertor and CIII light intensity and (b) the time trace of the C^{2+} flow velocity in the ELMy H-mode discharge (shot no. 34542).

V. SUMMARY AND DISCUSSION

A new Doppler coherence imaging spectroscopy interferometer for the 2D measurement of carbon ion line-of-sight flow in the

SOL has been developed on the HL-2A tokamak. A custom optical system and a dedicated calibration system have been applied for this interferometer. The spatial resolution is up to ~ 0.8 mm in the horizontal direction and ~ 9 mm in the vertical direction, over a 34° field of view. The robustness of group delay calibration and the feasibility of the extrapolation model for the fringe pattern calibration are demonstrated. The typical time resolution of the HL-2A Doppler CIS system is about 1 ms, which is higher than the time resolution of Doppler CIS systems viewing SOL on other conventional tokamaks. This feature allows for time-resolved 2D measurements in short-time phenomena on HL-2A. To show its high time-resolved measurement capability, the initial experimental results of this CIS interferometer during ELMs are reported.

Tomographic inversion of the CIS measurements to obtain the local emissivity and flow velocity is postponed to future work. Note that the correction of optical aberrations is very important for the tomographic inversion. The aberration introduced by the CIS lenses⁴³ is estimated to be no more than 1 pixel at the edge of flow velocity images. The aberration could also be affected by the position and orientation of the whole instrument with respect to the tokamak. The optical aberration correction is postponed to future work.

The wall reflection issue on the CIS measurement is not considered in this paper. The asymmetry of the carbon flow and intensity on the upper side and the lower side during an ELM crash need further investigation. Besides, to avoid the need for spectral lamps and phase extrapolation modeling, the installation of the calibration system on the HL-2A for regularly automatic phase calibration is also scheduled. In the longer term, it is planned that CIS diagnostics are to be applied to the HL-2M tokamak,⁴⁴ which is a new tokamak scheduled to operate since 2020, to explore high-performance plasma operation regimes.

ACKNOWLEDGMENTS

The authors would like to thank the HL-2A team and especially thank Dr. Xuantong Ding, Cheng Qiyun, Gong Shaobo, Chen Wenjin, He Xiaoxue, Li Bo, Fang Kairui, Li Yonggao, Bai Xingyu, Wei Huiling, Zhu Yuxuan, Yuan Jinbang, Chen Yihang, Yan Qinghao, Liu Hao, and Ting Wu for their help. The authors would also like to acknowledge helpful discussions with Dr. J. Harrison, Dr. N. Conway, and Professor P. H. Diamond.

This work was supported by the National Key R&D Program of China under Grant Nos. 2017YFE0301201, 2018YFE0309103, and 2018YFE0303100 and the National Natural Science Foundation of China under Grant Nos. 11905050, 11705052, 11875124, and U1867222. This work was also supported by the Engineering and Physical Sciences Research Council (Grant No. EP/L01663X/1) and a Royal Society International Exchanges 2015 Cost Share China award (Grant No. IE150624). This work was carried out within the framework of the EUROfusion Consortium and has received funding from the Euratom Research and Training Programme 2014–2018 under Grant Agreement No. 633053 and from the RCUK (Grant No. EP/T012250/1). The views and opinions expressed herein do not necessarily reflect those of the European Commission.

DATA AVAILABILITY

The data that support the findings of this study are available from the corresponding author upon reasonable request.

REFERENCES

- 1 M. Shimada, D. J. Campbell, V. Mukhovatov, M. Fujiwara, N. Kirneva, K. Lackner, M. Nagami, V. D. Pustovitov, N. Uckan, J. Wesley *et al.*, *Nucl. Fusion* **47**(6), S1–S17 (2007).
- 2 B. LaBombard, J. E. Rice, A. E. Hubbard, J. W. Hughes, M. Greenwald, J. Irby, Y. Lin, B. Lipschultz, E. S. Marmor, C. S. Pitcher *et al.*, *Nucl. Fusion* **44**(10), 1047 (2004).
- 3 N. Asakura, *J. Nucl. Mater.* **363–365**, 41–51 (2007).
- 4 G. F. Matthews, S. K. Erents, W. Fundamenski, C. Ingesson, R. D. Monk, and V. Riccardo, *J. Nucl. Mater.* **290–293**, 668–672 (2001).
- 5 G. S. Kirnev, G. Corrigan, D. Coster, S. K. Erents, W. Fundamenski, G. F. Matthews, and R. A. Pitts, *J. Nucl. Mater.* **337–339**, 271–275 (2005).
- 6 N. Asakura, H. Takenaga, S. Sakurai, G. D. Porter, T. D. Rognlien, M. E. Rensink, K. Shimizu, S. Higashijima, and H. Kubo, *Nucl. Fusion* **44**(4), 503–512 (2004).
- 7 E. J. Doyle, W. A. Houlberg, Y. Kamada, V. Mukhovatov, T. H. Osborne, A. Polevoi, G. Bateman, J. W. Connor, J. G. Cordey, T. Fujita *et al.*, *Nucl. Fusion* **47**(6), S18 (2007).
- 8 Z. Yan, G. McKee, R. Fonck, P. Gohil, R. Groebner, and T. Osborne, *Phys. Rev. Lett.* **112**(12), 125002 (2014).
- 9 N. Wang, Y. Liang, V. Igocine, W. Suttrop, L. Li, M. Maraschek, M. Bernert, P. Denner, M. Fritsch, S. Fietz *et al.*, *Nucl. Fusion* **59**(5), 054002 (2019).
- 10 T. E. Evans, R. A. Moyer, K. H. Burrell, M. E. Fenstermacher, I. Joseph, A. W. Leonard, T. H. Osborne, G. D. Porter, M. J. Schaffer, P. B. Snyder *et al.*, *Nat. Phys.* **2**(6), 419–423 (2006).
- 11 Y. Liu, A. Kirk, L. Li, Y. In, R. Nazikian, Y. Sun, W. Suttrop, B. Lyons, D. Ryan, S. Wang *et al.*, *Phys. Plasmas* **24**(5), 056111 (2017).
- 12 J. Howard, C. Michael, F. Glass, and A. Danielsson, *Plasma Phys. Controlled Fusion* **45**(7), 1143–1166 (2003).
- 13 J. Howard, *Rev. Sci. Instrum.* **77**(10), 10F111 (2006).
- 14 J. Howard, *Rev. Sci. Instrum.* **70**(1), 368–371 (1999).
- 15 J. Howard, *J. Phys. B: At., Mol. Opt. Phys.* **43**(14), 144010 (2010).
- 16 J. Howard, *Plasma Phys. Controlled Fusion* **50**(12), 125003 (2008).
- 17 O. Lischtschenko, K. Bystrov, G. D. Temmerman, J. Howard, R. J. E. Jaspers, and R. König, *Rev. Sci. Instrum.* **81**(10), 10E521 (2010).
- 18 R. Lester, Y. Zhai, C. Corr, and J. Howard, *Plasma Sources Sci. Technol.* **25**(1), 015025 (2016).
- 19 M. Nishiura, Z. Yoshida, N. Kenmochi, T. Sugata, K. Nakamura, T. Mori, S. Katsura, K. Shirahata, and J. Howard, *Nucl. Fusion* **59**(9), 096005 (2019).
- 20 J. Howard, C. Michael, F. Glass, and A. D. Cheetham, *Rev. Sci. Instrum.* **72**(1), 888–897 (2001).
- 21 J. Chung, R. König, J. Howard, M. Otte, and T. Klinger, *Plasma Phys. Controlled Fusion* **47**(6), 919–940 (2005).
- 22 D. Gradic, V. Perseo, R. König, and D. Ennis, *Fusion Eng. Des.* **146**, 995–998 (2019).
- 23 J. Chung, J. Ko, J. Howard, C. Michael, G. Von Nessi, A. Thorman, and M. De Bock, *J. Korean Phys. Soc.* **65**(8), 1257–1260 (2014).
- 24 J. Howard, R. Jaspers, O. Lischtschenko, E. Delabie, and J. Chung, *Plasma Phys. Controlled Fusion* **52**(12), 125002 (2010).
- 25 O. P. Ford, J. Howard, and R. C. Wolf, *Rev. Sci. Instrum.* **86**(9), 093504 (2015).
- 26 J. Howard, A. Diallo, M. Creese, B. D. Blackwell, S. L. Allen, R. M. Ellis, G. D. Porter, W. Meyer, M. E. Fenstermacher, N. H. Brooks *et al.*, *Rev. Sci. Instrum.* **81**(10), 10E528 (2010).
- 27 J. Howard, A. Diallo, M. Creese, S. L. Allen, R. M. Ellis, W. Meyer, M. E. Fenstermacher, G. D. Porter, N. H. Brooks, M. E. Van Zeeland *et al.*, *Contrib. Plasma Phys.* **51**(2–3), 194–200 (2011).
- 28 S. A. Silburn, J. R. Harrison, J. Howard, K. J. Gibson, H. Meyer, C. A. Michael, and R. M. Sharples, *Rev. Sci. Instrum.* **85**(11), 11D703 (2014).

- ²⁹D. Gradic, O. P. Ford, A. Burckhart, F. Effenberg, H. Frerichs, R. König, T. Lunt, V. Perseo, and R. C. Wolf, *Plasma Phys. Controlled Fusion* **60**(8), 084007 (2018).
- ³⁰I. Waters, H. Frerichs, S. Silburn, Y. Feng, J. Harrison, A. Kirk, and O. Schmitz, *Nucl. Fusion* **58**(6), 066002 (2018).
- ³¹J. Howard, M. Kocan, S. Lisgo, and R. Reichle, *Rev. Sci. Instrum.* **87**(11), 11E561 (2016).
- ³²M. Xu, X. R. Duan, Y. Liu, X. M. Song, D. Q. Liu, Y. Q. Wang, B. Lu, Q. W. Yang, G. Y. Zheng, X. T. Ding *et al.*, *Nucl. Fusion* **59**(11), 112017 (2019).
- ³³See <https://www.sigma-global.com/en/> for Global Web site of SIGMA.
- ³⁴W. H. Steel, *Interferometry* (CUP Archive, 1983), Vol. 1.
- ³⁵M. Françon and S. Mallick, *Polarization interferometers: applications in microscopy and macroscopy* (Wiley-Interscience, 1971).
- ³⁶S. Silburn, "A Doppler coherence imaging diagnostic for the mega-amp spherical tokamak," Ph.D., Durham University, 2014.
- ³⁷A. Kramida, Y. Ralchenko, J. Reader, and NIST ASD Team, NIST Atomic Spectra Database (ver. 5.7.1) (online), available: <https://physics.nist.gov/asd> (May 8, 2020), National Institute of Standards and Technology, Gaithersburg, MD, <https://doi.org/10.18434/T4W30F>.
- ³⁸L. Liu, D. L. Yu, W. J. Chen, X. F. He, X. X. He, Y. L. Wei, D. Li, Z. C. Yang, J. M. Gao, Y. G. Li *et al.*, *Fusion Eng. Des.* **143**, 41–47 (2019).
- ³⁹S. L. Allen, C. M. Samuell, W. H. Meyer, and J. Howard, *Rev. Sci. Instrum.* **89**(10), 10E110 (2018).
- ⁴⁰H. Hongda, Z. Jinhua, D. Jiaqi, and L. Qiang, *Plasma Sci. Technol.* **8**(4), 397–401 (2006).
- ⁴¹C. M. Samuell, S. L. Allen, W. H. Meyer, and J. Howard, *J. Instrum.* **12**(08), C08016 (2017).
- ⁴²See <http://www.agoptics.com/Alpha-BBO.html> for Alpha-BBO.
- ⁴³See https://www.sigma-global.com/en/lenses/cas/product/sports/s_70_200_28/data/ for Sigma lens performance data.
- ⁴⁴D. Q. Liu, H. Ran, G. S. Li, L. J. Cai, Z. Cao, H. Zou, Y. Li, J. Liu, Y. Qiu, T. Qiao *et al.*, *Fusion Eng. Des.* **88**(6), 679–682 (2013).